

Cite this: *Dalton Trans.*, 2022, **51**, 16861

# Aromatic amine electrochemical sensors based on a Co-MOF: a hydrogen bond-induced specific response†

Xiao-qin Wu, <sup>a</sup> Ze-yu Yang, <sup>a</sup> Xiao-jie Sang, <sup>a</sup> Xin-xin Tian <sup>\*b</sup> and Xuehong Wei<sup>\*a</sup>

A 2D Co-MOF,  $\{[\text{Co}_2(\text{L}^{2-})_2(\text{bipy})](\text{DMA})\cdot 2\text{H}_2\text{O}\}_n$  (**Co-1**,  $\text{H}_2\text{L} = 2,5$ -thienedioic acid; bipy = 2,2'-bipyridine; DMA = *N,N'*-dimethyl acetamide), was synthesized by hydrothermal method. **Co-1** has excellent air stability. When modifying the surface of a glassy carbon electrode (GCE) with **Co-1**, the obtained electrochemical sensor **Co-1**/GCE shows excellent sensitivity towards 1,3-dinitrobenzene (*m*-DNB) and 2,4-dinitroaniline (2,4-DNA), although the electrochemical conductivity of **Co-1** is not that good. The detection limits were as low as 0.0286  $\mu\text{M}$  and 0.161  $\mu\text{M}$ , respectively. DFT studies showed that the main interaction between **Co-1** and the guest molecules is *via* hydrogen bonding, formed by the  $-\text{NO}_2$  group and the coordinated  $\text{H}_2\text{O}$  molecule from the **Co-1** skeleton. Furthermore, the characteristic signals of both *m*-DNB and 2,3-DNA can still be observed in a mimicked industrial waste-water system containing 17 kinds of organic interferents, indicating high selectivity of the **Co-1**/GCE sensor.

Received 27th June 2022,  
Accepted 17th October 2022

DOI: 10.1039/d2dt02049a

rsc.li/dalton

## Introduction

Aromatic amine compounds are a class of important amine substances, which are important raw materials used in industrial production to make plastics, rubber and medicines. However, most of them have high toxicity and a stable chemical structure, and are difficult to degrade. Their improper discharge and leakage will cause serious pollution to the atmosphere and water resources, both of which are public health problems that countries all over the world attach great importance to resolving.<sup>1,2</sup> Many technological means can be applied to the detection of aromatic amine derivatives, such as gas chromatography,<sup>3</sup> fluorescence spectroscopy,<sup>4</sup> ultraviolet spectrophotometry<sup>5</sup> and liquid chromatography,<sup>6</sup> and so on. Most of these methods have drawbacks such as high cost, long analysis time and tedious operation. Therefore, the development of simple, rapid and sensitive methods for the detection of aromatic amine pollutants is still the focus of research work at the present stage.

Metal-organic frameworks (MOFs) are a kind of organic-inorganic hybrid crystalline material with metal ions as the center and organic linkers as ligands. They have many advantages, such as abundant pores, large specific surface areas, many active sites, and easy functionalization.<sup>7,8</sup> In the last decade, electrochemical sensors based on MOFs have been developed rapidly in the field of chemical detection and are widely used in biomedical and environmental science, and materials chemistry.<sup>9-12</sup> In 2018, Stefano Farris and coworkers designed an electrochemical sensor based on multi-walled carbon nanotubes, chitosan and gold nanoparticle (AuNP)-modified glassy carbon electrodes. Cyclic voltammetry (CV) methods were used for the quantitative detection of 2,4-diaminotoluene with a low detection limit of 35 nM.<sup>13</sup> The Akash Deep research group constructed an electrochemical sensor based on composite materials including Cu-MOFs, graphene and polyaniline. This composite material shows high porosity and excellent electrical conductivity. The sensor was applied to the detection of ammonia in aqueous solution with a detection limit of 0.6 ppm, within a concentration range of 1–100 ppm.<sup>14</sup> In 2020, Hongming He and coworkers designed two electrochemical sensors based on a Ag-MOF. It exhibited physicochemical stability and superior electrochemical activity for ultra-trace amounts of penicillin with a low detection limit of 0.849  $\text{pg mL}^{-1}$ .<sup>15</sup>

Electrochemical sensors based on MOFs are normally prepared by doping or post-modification methods. Due to the high-dimensional skeleton and ordered porous structure of

<sup>a</sup>Scientific Instrument Center, Shanxi University, Taiyuan 030006, China.  
E-mail: xhwei@sxu.edu.cn

<sup>b</sup>Institute of Molecular Science, Key Laboratory of Materials for Energy Conversion and Storage of Shanxi Province, Key Laboratory of Chemical Biology and Molecular Engineering of Education Ministry, Shanxi University, Taiyuan 030006, China.  
E-mail: tianxx@sxu.edu.cn

† Electronic supplementary information (ESI) available. CCDC 2174693. For ESI and crystallographic data in CIF or other electronic format see DOI: <https://doi.org/10.1039/d2dt02049a>

MOFs, suitable metal ions and organic ligands with special functional groups can be anchored onto or penetrated into the materials. However, most of these materials have low electrochemical activity or poor stability, and have to be combined with electrochemically active substances such as polyacids, carbon nanotubes or gold nanoparticles to improve the performance of sensors. Only a few MOFs have overcome the above disadvantages and can be directly applied to sensors without post-modification.<sup>16–18</sup> Therefore, to further simplify the sensor preparation process, designing MOFs with both high electrochemical activity and stability is a great challenge to scientists. In addition, due to the differences in ligand types, metal center types and coordination modes, MOFs show various structural and electronic characteristics. The corresponding interactions between MOFs as electrochemical sensors and small guest molecules are also varied. Figuring out the decisive structural or electronic properties of MOFs for a better sensor performance is also an urgent and important subject.

Herein, based on our previous work experience,<sup>19,20</sup> a 2D Co-MOF,  $\{[\text{Co}_2(\text{L}^{2-})_2(\text{bipy})](\text{DMA})\cdot 2\text{H}_2\text{O}\}_n$  (**Co-1**,  $\text{H}_2\text{L} = 2,5$ -thiendioic acid; bipy = 2,2'-bipyridine; DMA = *N,N'*-dimethyl acetamide), was designed and synthesized by a hydrothermal method. **Co-1** showed excellent thermal stability and electrochemical activity. Using **Co-1** to modify a glassy carbon electrode (GCE), the produced **Co-1/GCE** electrochemical sensor

was used to detect four aromatic amine compounds with similar sizes and properties: 1,3-dinitrobenzene (*m*-DNB), 2,4-dinitroaniline (2,4-DNA), 4-nitro-*o*-phenylenediamine (4-NOPD) and *p*-nitroaniline (*p*-NA) in a water system (Scheme 1). **Co-1** showed outstanding selectivity and sensitivity towards *m*-DNB or 2,4-DNA either in an environment with simple components or environments mixed with several interferences. Density functional theory (DFT) calculations were performed to study the interaction between **Co-1** and guest aromatic amine molecules.

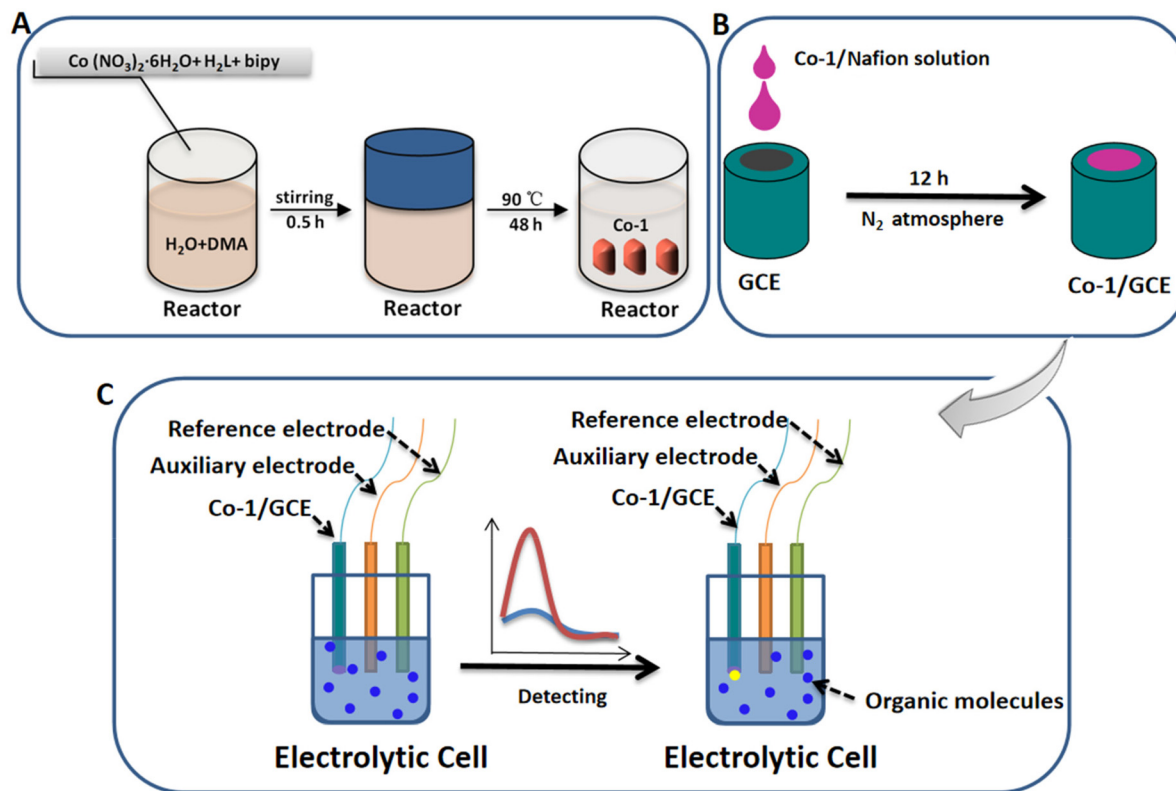
## Experimental

### Synthesis of $\{[\text{Co}_2(\text{L}^{2-})_2(\text{bipy})](\text{DMA})\cdot 2\text{H}_2\text{O}\}_n$ (**Co-1**)

$\text{Co}(\text{NO}_3)_2\cdot 6\text{H}_2\text{O}$  (58 mg, 0.2 mmol),  $\text{H}_2\text{L}$  (33 mg, 0.2 mmol) and bipy (31 mg, 0.2 mmol) were dissolved in a mixed solution with 5 mL of water and 10 mL of DMA. This solution was transferred slowly into a 23 mL Teflon-lined stainless steel reactor, maintained at 90 °C for 48 h in an oven and cooled at room temperature for 48 h. After that, the mixed solution was filtered and orange transparent block crystals were obtained. The yield was 54.12% (based on Co).

### Preparation of the **Co-1/GCE**

Prior to use, the GCE was polished carefully with 0.5 μm and 0.01 μm alumina slurry to obtain a mirror like surface, and



**Scheme 1** (A) Schematic of the **Co-1** synthesis process; (B) an enlarged view of preparing a **Co-1/GCE**; and (C) the electrochemical sensing process for recognizing organic molecules.

then ultrasonically cleaned with ultrapure water, nitric acid aqueous solution ( $v/v = 1 : 1$ ), sodium hydroxide aqueous solution ( $0.1 \text{ mol L}^{-1}$ ) and ethanol in turn to remove residual alumina on the surface, after that it was dipped in a clean beaker filled with ultrapure water. The ultrasonication process was handled with an ultrasonic cleaning machine (Elma, S100H). 2 mg of **Co-1** powder was ultrasonically dispersed into 200  $\mu\text{L}$  of Nafion solution for 2 h to prepare **Co-1/Nafion**, and this solution was put into a capsule and stored at 4  $^{\circ}\text{C}$  until use. 10  $\mu\text{L}$  of this stored solution was dripped onto the GCE surface and dried under a  $\text{N}_2$  atmosphere for 12 h and a **Co-1/GCE** was obtained. For impedance analysis, electrochemical impedance spectroscopy (EIS) was performed using a Chi660E electrochemical workstation (China). All samples were collected using the above three-electrode system in 0.1 mM  $[\text{Fe}(\text{CN})_6]^{4-/3-}$  buffer solution containing 0.1 M KCl, with the EIS frequency cycled between 0.1 Hz and 100 kHz.

## Results and discussion

### Structural analysis of Co-1

The single X-ray crystal diffraction data show that **Co-1** is crystallized in the triclinic crystal system,  $P\bar{1}$  space group. Its asymmetric unit consists of two Co(II) ions, two dehydrogenated 2,5-thiophene dicarboxylic acid ions  $\text{L}^{2-}$ , two water molecules

and one bipy molecule (Fig. 1A). The Co1 atom is tetra-coordinated by two N atoms of the bipy molecule and two carbonyl oxygen atoms of two different  $\text{L}^{2-}$  ions. The Co2 atom is hexa-coordinated by six O atoms from two water molecules and four carbonyl oxygen atoms of different  $\text{L}^{2-}$  ions. Co1 and Co2, with their coordination atoms, form a  $\{\text{Co}_2\text{N}_2\text{O}_8\}$  node, and form a 2D net structure by extending the  $x$  and  $y$  axes through  $\text{L}^{2-}$  ions (Fig. 1B). This 2D net structure penetrates through weak intermolecular interactions. Following the ABAB (A and B have the same structure) packing arrangement along the  $z$ -axis, **Co-1** can form a one-dimensional rhombus channel structure with a pore size of  $16 \text{ \AA} \times 10 \text{ \AA}$  (Fig. 1C and D).

The stability of electrode-modified materials is very important in electrochemical experiments. In this work, the XRD pattern of **Co-1** placed in air for two weeks was compared with that of a simulated single crystal diffraction to confirm its purity (Fig. 2A). It was found that the peak position of **Co-1** was basically similar to the simulated one, which exhibits high purity and air stability. To check the stability of **Co-1** in water, the PXRD of **Co-1** after immersing it in water for 1 h was obtained. As shown in Fig. S1,<sup>†</sup> the graph is also similar to the simulated one, indicating the good water stability of **Co-1**. Thermogravimetric analysis (TGA) results show that the weight loss of about 3% observed between 0 and 100  $^{\circ}\text{C}$  was ascribed to volatilization of two water molecules and the weight loss of 19.7% observed between 100 and 200  $^{\circ}\text{C}$  was ascribed to vol-

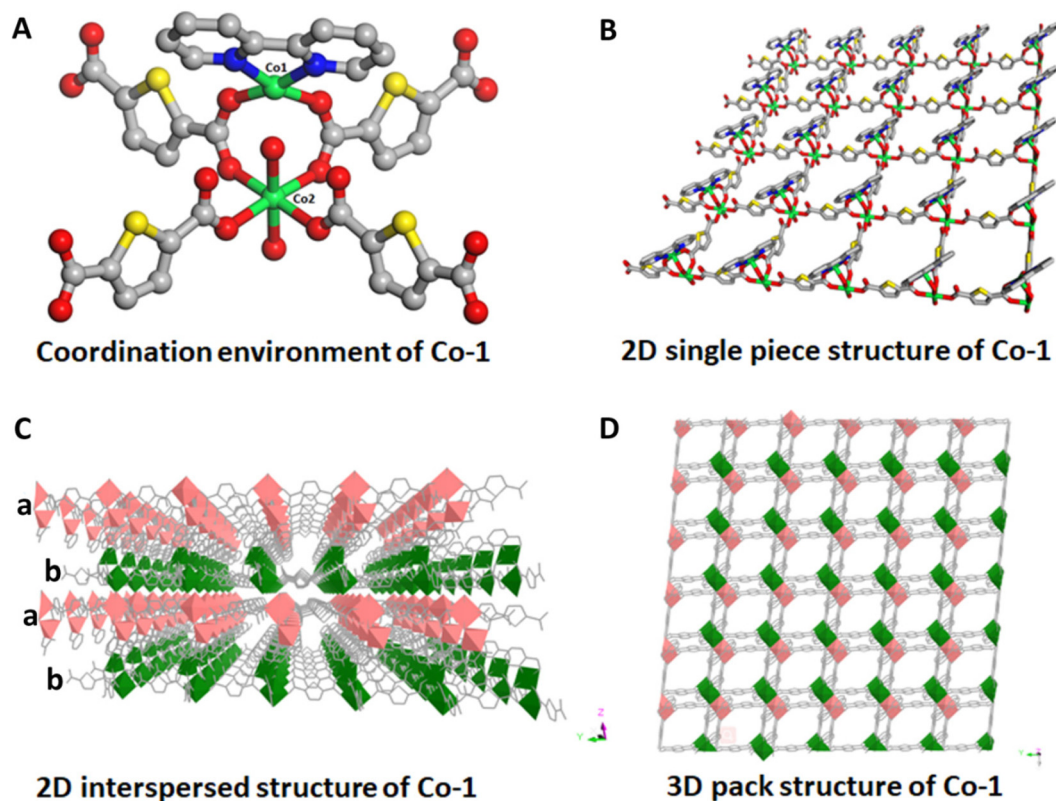


**Fig. 1** (A) Coordination environment of Co-1; (B) 2D single piece structure of Co-1; (C) interspersed structure of Co-1; (D) 3D pack structure of Co-1 along the  $z$ -axis.

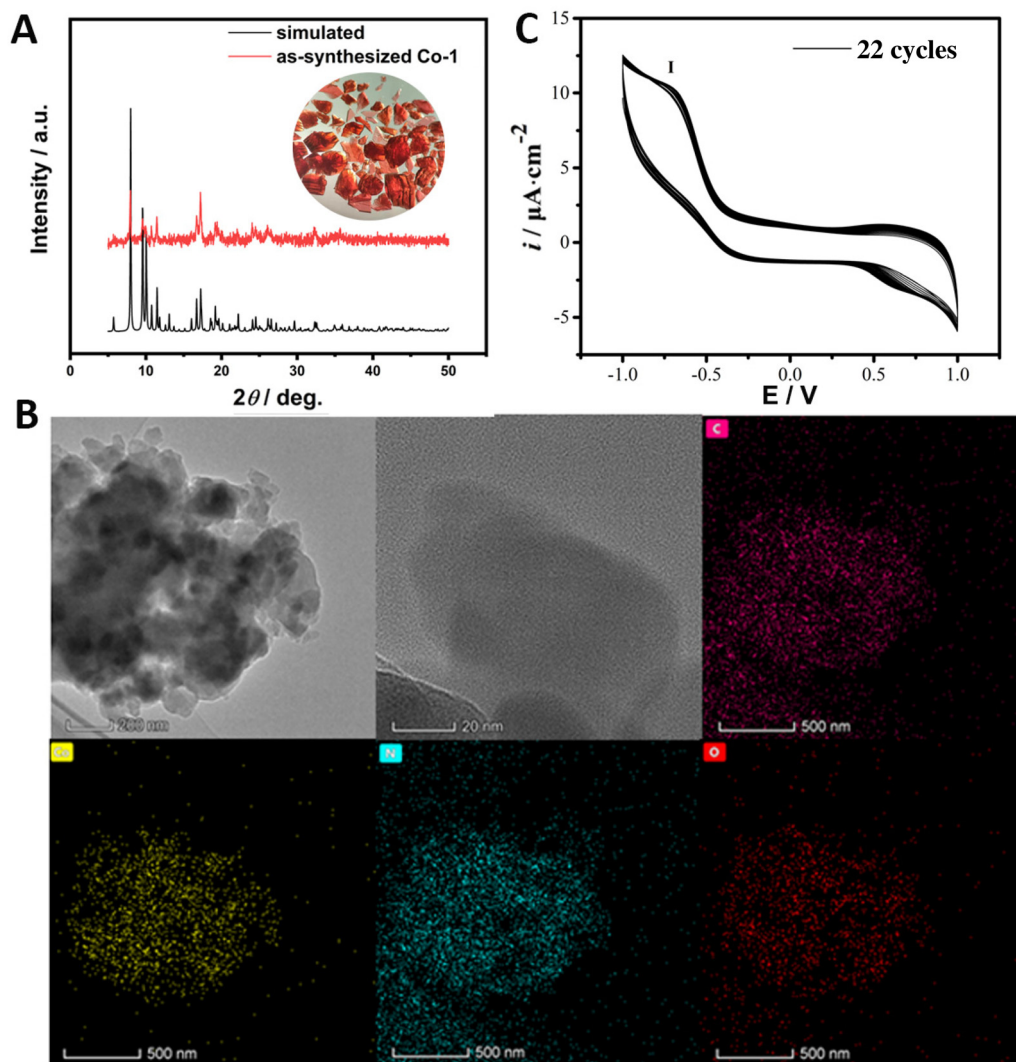


Fig. 2 (A) PXRD graphs of Co-1; (B) TEM image and elemental mapping of the dispersed micro crystals of Co-1; (C) the chemical stability tests: CVs of Co-1/GCE in PBS (pH = 6.86) for 22 circles.

utilization of one DMA molecule in the lattice. When the temperature is in the range from 200 to 300 °C, the curve is in the platform stage, indicating that Co-1 can exist stably in this temperature range, but when the temperature reaches 350 °C, the curve drops sharply, and Co-1 crystals begin to decompose (Fig. S2†). These results show that Co-1 has excellent thermal stability. It is suggested Co-1 reaches the requirements of an electrode-modifying material and can be used to assemble an electrochemical sensor. The morphology of Co-1 was characterized by transmission electron microscopy (TEM). The TEM image and elemental mapping of the dispersed micro-crystals of Co-1 are shown in Fig. 2B. At low magnification, TEM images of Co-1 showed stacked blocks, while high magnification showed nanoscale lamellar structures.

Since carboxylate-based MOFs are not stable in highly concentrated phosphate-containing aqueous solutions, a pre-treatment of Co-1 using Nafion was conducted in this work. Nafion is an organic polymer with a strong resistance to chemical cor-

rosion. We observed the changes of Co-1 and Nafion-protected Co-1 by immersing both in PBS solution under a microscope (Fig. S3†). It is found that Co-1 was quickly decomposed in PBS solution (<6 min), but the gel properties of Nafion effectively delays the decomposition of the Co-MOF, and the structure of Co-1 is still clearly visible after one hour. The PXRD graphics of Co-1@Nafion after immersing in PBS for 0.5 h and 1 h, respectively, are given in Fig. S4.† It can be seen that the crystal structure of Co-MOFs immersed in PBS is well maintained even though the peak intensity decreased. Therefore, we suggest that Co-1/Nafion has good tolerance for a short electrochemical experiment time and is suitable for detection sensing.

#### Electrochemical characterization of Co-1

To characterize the charge-transfer resistance ( $R_{ct}$ ) of Co-1/GCE, EIS tests were performed on bare GCE or Co-1/GCE at a frequency of 0.1–100 kHz in 0.1 mM  $[\text{Fe}(\text{CN})_6]^{4-/3-}$  buffer solu-

tion containing 0.1 M KCl (Fig. S6†). The diameter of the semi-circle represents the charge transfer resistance and the  $R_{ct}$  value of bare GCE and Co-1/GCE were 0.01  $\Omega$  and 15.55  $\Omega$ , respectively. This shows that Co-1 has been successfully immobilized on the GCE surface. Furthermore, the higher  $R_{ct}$  value of Co-1/GCE indicates that the electrical conductivity of Co-1 is not that good. This may be attributed to the intrinsic insulating nature of the carboxylate bonds utilized to form MOFs.

The electrochemical stability of Co-1/GCE was measured by CVs for a further 22 cycles. The peak current density  $I$  at  $-0.72$  V ( $E_{p,i}$ ) almost did not decrease as the scan cycle numbers rise, indicating good reproducibility that originated from the high stability of Co-1 (Fig. 2C). The influence of scan rates ( $\nu$ ) was also investigated. The CV tests of Co-1/GCE in phosphate buffer solution (PBS, pH = 6.8) with a scan rate from 0.02 V s<sup>-1</sup> to 0.18 V s<sup>-1</sup> are shown in Fig. S7.† The oxidation peak current density ( $i_{p,i}$ ) is directly proportional to  $\nu^{1/2}$  (Fig. S8†), which indicates a diffusion-controlled process. The electrochemical active surface area (ECSA) of Co-1/GCE was calculated as 1.242 cm<sup>2</sup> according to the Randles-Sevcik equation:<sup>21</sup>  $i_p = 268600n^{2/3}AD^{1/2}C\nu^{1/2}$ , where  $i_p$  is the peak  $I$  current density (A cm<sup>-2</sup>),  $n$  is the number of electrons transferred ( $n = 1$ , in this case),  $A$  is the electrochemical active surface area (cm<sup>2</sup>),  $D$  is

the diffusion coefficient in cm<sup>2</sup> s<sup>-1</sup> ( $6.70 \times 10^{-6}$  cm<sup>2</sup> s<sup>-1</sup>),  $C$  is the concentration in mol L<sup>-1</sup> (0.005 M K<sub>3</sub>Fe(CN)<sub>6</sub>) and  $\nu$  is the scan rate (V s<sup>-1</sup>). It indicated that Co-1 has a large ECSA, showing excellent electrochemical stability and reproducibility, which promise its good sensing property.

Aromatic amine compounds as a class of important aniline derivatives are often used as raw materials for industrial or agricultural applications. They also can cause serious damage to the nervous system and organs of animals or people, and may lead to cancer.<sup>22</sup> Consequently, detecting and recognizing these compounds in environmental systems is of great significance to public health and life safety.

Co-1/GCE was used as an electrochemical sensor for detecting four aromatic amine compounds of similar structure, 1,3-dinitrobenzene (*m*-DNB), 2,4-dinitroaniline (2,4-DNA), 4-nitro-*o*-phenylenediamine (4-NOPD) and *p*-nitroaniline (*p*-NA) in a water system. Firstly, blank tests were performed on bare GCE and Nafion/GCE for detecting *m*-DNB, 2,4-DNA, 4-NOPD or *p*-NA (Fig. S10 and S11†). The results showed that these four organic molecules generate almost no response on either a bare GCE or Nafion/GCE. Furthermore, CV was carried out on Co-1/GCE in PBS (pH = 6.86) in the presence of 0.5 mM *m*-DNB, 2,4-DNA, 4-NOPD or *p*-NA, respectively. As shown in

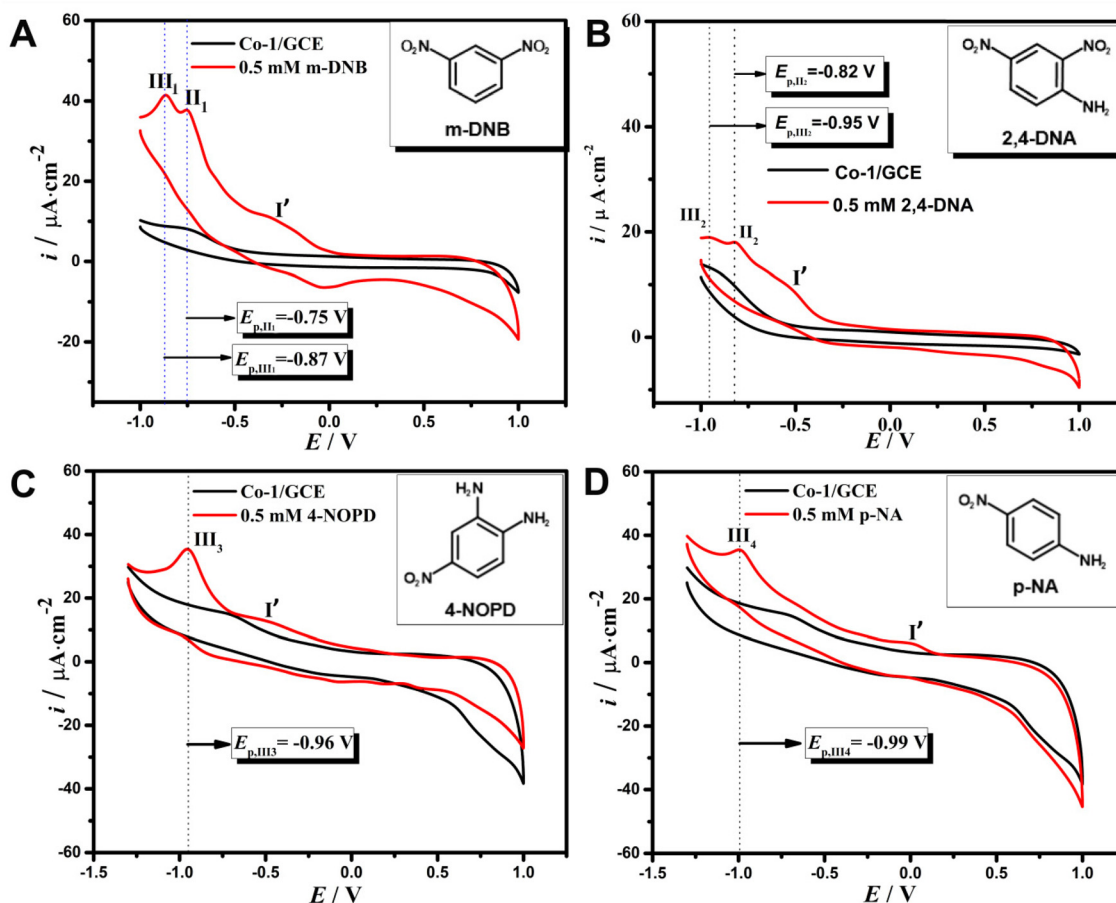


Fig. 3 CVs at Co-1/GCE in PBS (pH = 6.86) with or without 0.5 mM *m*-DNB (A), 2,4-DNA (B), 4-NOPD (C) and *p*-NA (D), respectively.

Fig. 3, the peak potential  $I'$  belongs to **Co-1**, but also it can be seen to slightly shift to lower potentials, which might be because the interaction between guest molecules and the **Co-1** substrate lowers the system energy. There are two obvious oxidation peaks near the peak potential,  $E_{p,III} = -0.75$  V and  $E_{p,III} = -0.87$  V (Fig. 3A), which were observed during *m*-DNB detection. For the 2,4-DNA detection shown in Fig. 3B, two oxidation peaks also appeared near these positions ( $E_{p,II} = -0.82$  V and  $E_{p,III} = -0.96$  V). Both peak current densities of *m*-DNB

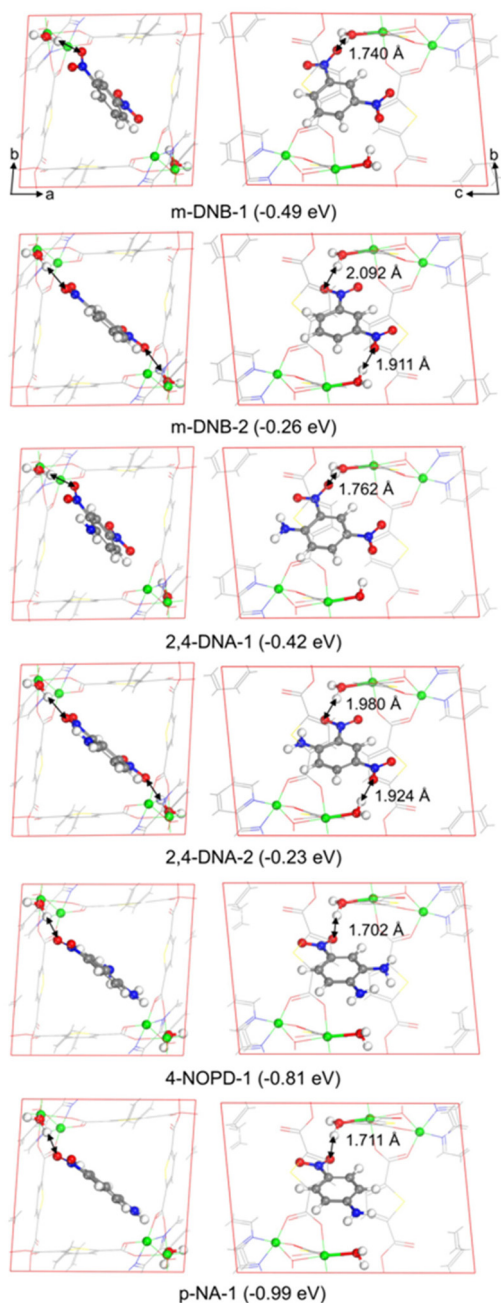


Fig. 4 The structures and adsorption energies of *m*-DNB, 2,4-DNA, 4-NOPD and *p*-NA interacting with the MOF skeleton through one or two  $-\text{NO}_2$  groups by hydrogen bonding (views from different directions).

were about twice as strong than those of 2,4-DNA. However, there is only one oxidation peak with a peak position near  $-1.0$  V for 4-NOPD and *p*-NA (Fig. 3C and D).

To figure out the origin of the oxidation peaks over a potential range from  $-1.0$  to  $-0.75$  V, density functional theory (DFT) calculations were performed to study the possible interaction mode of the four guest molecules with the **Co-1** substrate (Fig. 4). It is found that the  $-\text{NO}_2$  group of *m*-DNB can interact with the  $\text{H}_2\text{O}$  molecule that is coordinated with the Co2 atom on the MOF framework, and form one stable hydrogen bond (*m*-DNB-1, 1.740 Å) or two weak hydrogen bonds (*m*-DNB-2, 2.092 Å and 1.911 Å). The adsorption energy of these two structures is  $-0.49$  eV and  $-0.26$  eV, respectively. Similarly, the 2,4-DNA also interacts with the **Co-1** substrate through one or two  $-\text{NO}_2$  groups by forming one stable hydrogen bond (2,4-DNA-1, 1.762 Å) or two weak hydrogen bonds (2,4-DNA-2, 1.980 Å and 1.924 Å).

The adsorption energies of these two structures are  $-0.42$  eV and  $-0.23$  eV, respectively. Obviously, the adsorption energies of *m*-DNB/**Co-1** and 2,4-DNA/**Co-1** systems are very close in both interaction modes, and the structure with only one hydrogen bond ( $-\text{ONO}\cdots\text{HOH}-\text{Co}^{2-}$ ) is thermodynamically more favorable than that with two hydrogen bonds. However, for 4-NOPD and *p*-NA, there is only one  $-\text{NO}_2$  group, and the distance of the corresponding hydrogen bond (1.702 and 1.711 Å, respectively) is shorter than that of the former two molecules.

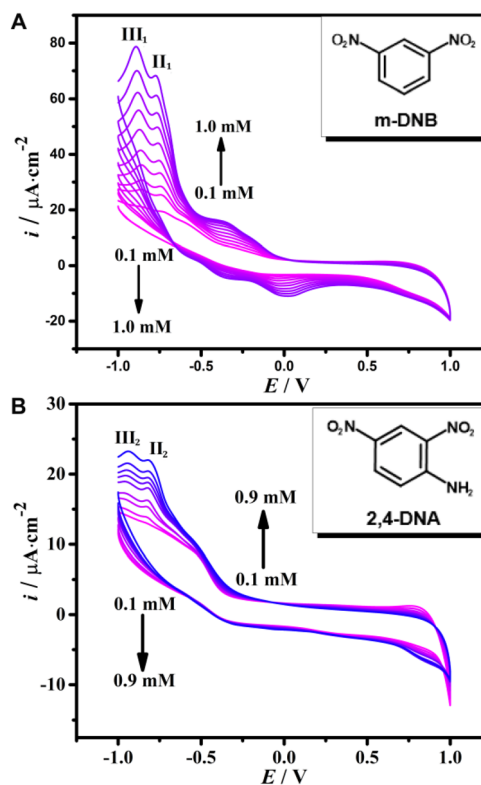


Fig. 5 (A) CVs at **Co-1**/GCE in PBS (pH = 6.86) with different *m*-DNB concentrations from 0.1 to 1.0 mM; (B) CVs at **Co-1**/GCE in PBS (pH = 6.86) with different 2,4-DNA concentrations from 0.1 to 0.9 mM, scan rate  $0.1$  V  $\text{s}^{-1}$ .

The adsorption energies ( $-0.81$  and  $-0.99$  eV, respectively) are much lower than those of *m*-DNB and 2,4-DNA. We attribute the differences in adsorption energy to a combination of molecule size and electronic effects. Based on these results, we suppose that the oxidation peak correlates with the  $-\text{NO}_2$  group of the guest molecule. The guest molecule with one  $-\text{NO}_2$  group can interact with the **Co-1** substrate through one hydrogen bond and leads to one oxidation peak. The guest molecule with two  $-\text{NO}_2$  groups has two interaction modes with the **Co-1** substrate through one or two hydrogen bonds and, therefore, this leads to two oxidation peaks. It should also be mentioned that the  $-\text{NH}_2$  group of the guest molecule can also interact with the **Co-1** substrate by forming a hydrogen bond with the O atom on the MOF framework or the O atom of  $\text{H}_2\text{O}$  (Fig. S9<sup>†</sup>). Different from the donating properties of the  $-\text{NO}_2$  group, the  $-\text{NH}_2$  group withdraws electrons from the O atom of  $\text{H}_2\text{O}$  or skeleton O, indirectly decreasing the coordination of Co atoms. This reduction effect partially weakens the previous oxidation effect caused by the  $-\text{NO}_2$  group. For 2,4-DNA, the structures with both  $-\text{NO}_2$  and  $-\text{NH}_2$  groups interacting with the substrate (2,4-DNA-3, 2,4-DNA-4) are thermodynamically much more stable than those with only  $-\text{NO}_2$  interacting with the substrate (2,4-DNA-1, 2,4-DNA-2). However, for 4-NOPD and *p*-NA, the adsorption energies change little with or without  $-\text{NH}_2$  co-interaction. This may

explain the lower peak current densities when **Co-1**/GCE detects the latter three molecules, especially those for 2,4-DNA.

To sum up, the size of the guest molecule and the type, number, and the position of functional groups all play a crucial role in hydrogen bond formation and therefore affect the oxidation peaks. Although 4-NOPD and *p*-NA have obvious electrochemical response signals, they have only one oxidation peak signal, and are easily confused with other contaminants. Therefore, based on the double peak characteristic, the concentration influence on CVs for both *m*-DNB and 2,4-DNA were further investigated (Fig. 5). The current density of peak II<sub>1</sub> and peak III<sub>1</sub> of *m*-DNB increased gradually with an increase of the concentration. 2,4-DNA also shows the same trend. This showed that both of them can be quantitatively detected by this **Co-1** sensor. The influence of scan rates for both *m*-DNB and 2,4-DNA were also investigated (Fig. S14 and S16<sup>†</sup>). These exhibit a nearly linear variation *vs.* the square root of scan rates. The results suggested that the redox reactions of both *m*-DNB and 2,4-DNA were controlled by a mass transfer process.<sup>23</sup>

DPV is a method with lower background current densities. It is also a more sensitive method than traditional CV methods. Therefore, DPV was used to investigate the current response values of various concentrations of *m*-DNB and 2,4-

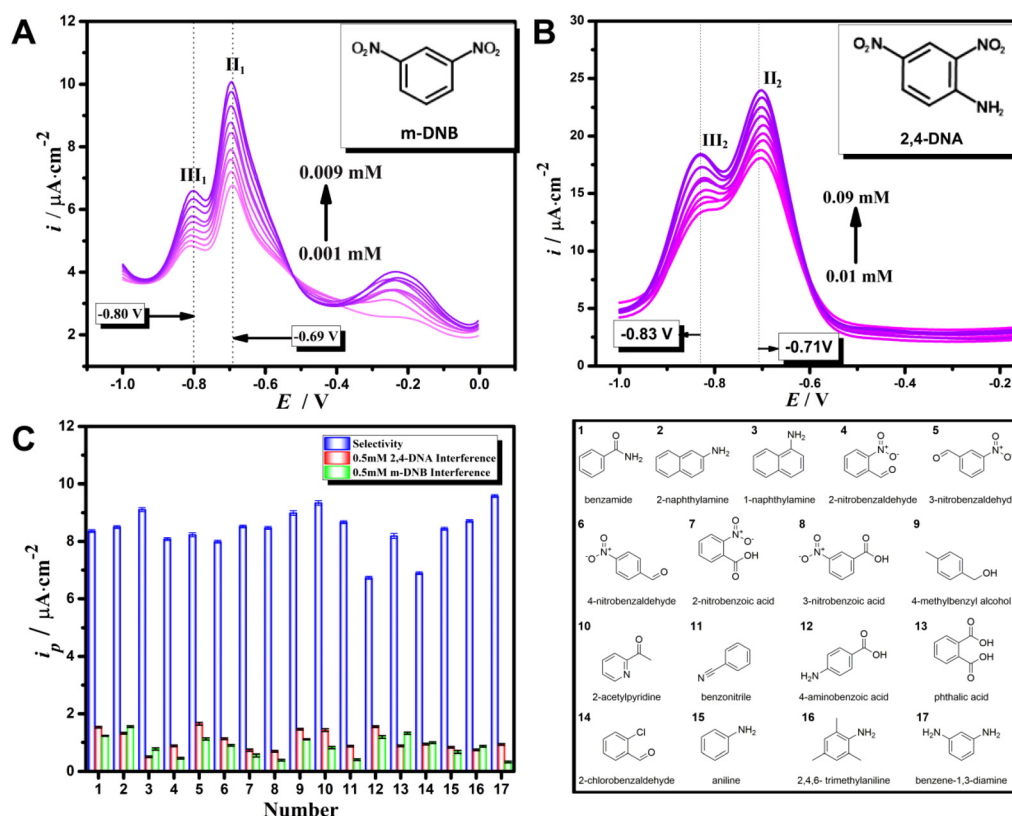


**Fig. 6** (A) DPV curves of **Co-1**/GCE in the PBS electrolyte containing different concentrations of *m*-DNB (concentration range 0.001–0.009 mM) at voltages ranging from 0 V to  $-1.0$  V; (B) DPV curves of **Co-1**/GCE in the PBS (pH = 6.86) electrolyte containing different concentrations of 2,4-DNA (concentration range 0.01–0.09 mM) at voltages ranging from  $-0.2$  V to  $-1.0$  V; (C) the bar columns based on selectivity and interference tests, and the structures of interferents 1–17.

DNA in PBS (pH = 6.86) (Fig. 6A and B). The oxidation peaks II<sub>1</sub> and III<sub>1</sub> can be detected clearly at nearby higher potentials of −0.69 V and −0.80 V, respectively. When increasing the *m*-DNB concentrations from 1 to 9 μM, the peak current densities of II<sub>1</sub> and III<sub>1</sub> gradually increased. The same situation is also shown in Fig. 6B, where the oxidation peaks II<sub>2</sub> and III<sub>2</sub> can be detected clearly at nearby higher potentials of −0.71 and −0.83 V, respectively, on increasing 2,4-DNA concentrations from 0.1 to 0.9 μM, and the peak current densities of II<sub>2</sub> and III<sub>3</sub> also gradually increase. The DPV plots of peak current densities II<sub>1</sub> and II<sub>2</sub> are shown in Fig. S18 and S19,† where *i*<sub>p,II1</sub> or *i*<sub>p,II2</sub> exhibits a nearly linear variation vs. the concentrations of *m*-DNB or 2,4-DNA following the below equations:

$$i_{p,II1} = 4.19 \times 10^{-6} C_{m\text{-DNB}} + 6.33 \times 10^{-7}, R^2 = 0.998 \quad (1)$$

$$i_{p,II2} = 74.4 \times 10^{-6} C_{2,4\text{-DNA}} + 17.3 \times 10^{-6}, R^2 = 0.999 \quad (2)$$

The limits of detection (LOD) for *m*-DNB or 2,4-DNA are 0.0286 μM and 0.161 μM, respectively. The LOD was calculated with the equation, LOD = 3σ/*M*, where *M* and σ are the slope of the calibration curve and standard deviation of the blank peak current (*n* = 10).<sup>24</sup> Compared with other method/sensor materials<sup>25–30</sup> (Table 1 and Table S2†), results show that the Co-1 sensor is advantageous in many aspects, including lower cost, easier preparation steps, simpler post-treatment, and so on.

### Selectivity and interference studies

Selectivity tests were performed with the Co-1/GCE sensor. A mimicked industrial waste-water system, containing 17 kinds of organic interferents, was used for this test. CV tests showed that the peak current densities of interferents 1–17, namely, benzamide, 2-naphthylamine, 1-naphthylamine, 2-nitrobenzaldehyde, 3-nitrobenzaldehyde, 4-nitrobenzaldehyde, 2-nitrobenzoic acid, 3-nitrobenzoic acid, 4-methylbenzyl alcohol, 2-acetylpyridine, benzonitrile, 4-aminobenzoic acid, phthalic acid, 2-chlorobenzaldehyde, aniline, 2,4,6-trimethylaniline and benzene-1,3-diamine, showed little change (Fig. S20†). Interference studies (Fig. S21 and S22†) showed that only *m*-DNB or 2,4-DNA could cause a considerable peak current density. The Δ*i*<sub>pII</sub> values, the differentials between the peak II current densities of *m*-DNB or 2,4-DNA and the current den-

sities of interferents 1–17 at the corresponding potential position, were small (Fig. 6C). These results demonstrated that the Co-1/GCE sensor has outstanding selectivity and excellent sensitivity for *m*-DNB or 2,4-DNA.

## Conclusions

In summary, a 2D Co-MOF with extremely excellent stability was successfully synthesized and used as an electrochemical sensor material for detecting *m*-DNB or 2,4-DNA in a water system. The electrochemical detecting positions for *m*-DNB were −0.82 V and −0.95 V with a low LOD of 0.161 μM. The electrochemical detecting positions for 2,4-DNA were −0.82 V and −0.95 V with a low LOD 0.161 μM. DFT calculations were used for explaining the interaction mechanism between the guest molecules and the MOF materials. It is found that the oxidation peak is mainly attributed to the interaction of the −NO<sub>2</sub> group with the Co<sup>2+</sup>-coordinated H<sub>2</sub>O molecule. Furthermore, the size of the guest molecule, the number of −NO<sub>2</sub> groups and the types of other co-existing groups all have an effect on the oxidation peak. In addition, Co-1/GCE shows outstanding selectivity towards *m*-DNB or 2,4-DNA in mixed solutions containing other interferents. Combined with DFT calculations, this work explains the interaction mechanism between electrically active MOFs and small guest molecules, and reveals the importance of H<sub>2</sub>O molecules on the MOF skeleton. These findings provide a promising way for the design and synthesis of novel electrochemical MOFs.

## Author contributions

The manuscript was written through contributions of all authors. All authors have given approval to the final version of the manuscript.

## Conflicts of interest

There are no conflicts to declare.

## Acknowledgements

This work was supported by the National Natural Science Foundation of China under grants (No. 21903049). We also acknowledge the Scientific Instrument Center of Shanxi University for providing the testing service of this work.

## References

- C. J. Zhang, H. Chen, G. Xue, Y. B. Liu, S. P. Chen and C. Jia, *J. Cleaner Prod.*, 2021, **321**, 128971.
- S. Chinthakindi and K. Kannan, *Environ. Int.*, 2021, **157**, 106840.

**Table 1** Comparison of different detection methods with respect to the recognition efficiency of 2,4-DNA

Method/materials	Detection range	LOD	Ref.
PMME-HPLC	0.135–10.8 nM	0.03 nM	25
DLLMEHPLC-DAD	0.11–54.61 nM	0.03 nM	26
HPLC-SPE-UVD	0.5–5.0 μM	4.50 nM	27
NanoMIPs	0.01–2.71 μM	7.0 nM	28
Cd <sup>2+</sup> -(pyridine-4-yl)-dpa-pta	0–160 ppm	1.63 mM	29
Fluorescence sensor/Zn(II)-Ln compound	0–0.1 μM	41.8 μM	30
Electrochemical sensor/Co-MOF	0.01 mM–0.09 mM	0.161 μM	This work

- 3 J. P. Zhu and B. Aikawa, *Environ. Int.*, 2004, **30**(2), 135–143.
- 4 X. L. Chen, Z. B. Li, Y. X. Zhu and J. G. Xu, *Anal. Chim. Acta*, 2004, **505**(2), 283–287.
- 5 X. P. Yu, L. Tan, Y. L. Yu, Y. Xia, Z. Guan, J. Gu, J. Wang, H. Chen and F. Jiang, *Chemosphere*, 2022, **287**, 132292.
- 6 M. Jayapal, H. Jagadeesan, V. Krishnasamy, G. Shanmugam, V. Muniyappan, D. Chidambaram and S. Krishnamurthy, *Environ. Pollut.*, 2022, **302**, 119009.
- 7 X. Y. Shi, Y. Y. Shan, M. Du and H. Pang, *Coord. Chem. Rev.*, 2021, **444**, 214060.
- 8 A. Dutta, Y. Pan, J. Q. Liu and A. Kumar, *Coord. Chem. Rev.*, 2021, **445**, 214074.
- 9 S. Zhang, F. L. Rong, C. A. P. Guo, F. H. Duan, L. H. He, M. H. Wang, Z. H. Zhang, M. M. Kang and M. Du, *Coord. Chem. Rev.*, 2021, **439**, 213948.
- 10 S. Tajik, H. Beitollahi, F. G. Nejad, I. Sheikhshoaie, A. S. Nugraha, H. W. Jang, Y. Yamauchi and M. Shokouhimehr, *J. Mater. Chem. A*, 2021, **9**(13), 8195–8220.
- 11 M. Z. Lv, W. Zhou, H. Tavakoli, C. Bautista, J. F. Xia, Z. H. Wang and X. J. Li, *Biosens. Bioelectron.*, 2021, **176**, 112947.
- 12 B. He and X. Yan, *Sens. Actuators, B*, 2020, **306**, 127558.
- 13 M. Ghaani, C. Rovera, F. Pucillo, M. R. Ghaani, R. T. Olsson, M. Scampicchio and S. Farris, *Sens. Actuators, B*, 2018, **277**(20), 477–483.
- 14 S. K. Bhardwaj, G. C. Mohanta, A. L. Sharma, K.-H. Kim and A. Deep, *Anal. Chim. Acta*, 2018, **1043**, 89–97.
- 15 H. He, S. Q. Wang, Z. Y. Han, X. H. Tian, W. W. Zhang, C. P. Li and M. Du, *Appl. Surf. Sci.*, 2020, **531**, 147342.
- 16 D. Gao, J. H. Chen, S. Fang, T. Ma, X. H. Qiu, J. G. Ma, Q. Gu and P. Cheng, *Mater.*, 2021, **4**(3), 1001–1016.
- 17 Y. Song, M. Xu, X. Liu, Z. Li, C. Wang, Q. Jia, Z. Zhang and M. Du, *Electrochim. Acta*, 2021, **368**, 137609.
- 18 X. Zhang, N. Qu, S. Yang, D. Lei, A. Liu and Q. Zhou, *Mater. Chem. Front.*, 2020, **5**, 482–491.
- 19 X. Q. Wu, P. Q. Feng, Z. Guo and X. Wei, *Langmuir*, 2020, **36**(46), 14123–14129.
- 20 X. Q. Wu, Y. Liu, P. Q. Feng, X. H. Wei, G. M. Yang, X. H. Qiu and J. G. Ma, *Chem. Commun.*, 2019, **55**(28), 4059–4062.
- 21 A. Natarajan and N. Mohankumar, *Comput. Chem.*, 1997, **21**(5), 315–318.
- 22 S. Prince and T. Suthan, *J. Electron. Mater.*, 2022, **51**(21), 1639–1652.
- 23 Y. X. Tong, P. Liu and Y. Q. Yang, *Electrochemistry of coordination compounds*, Guang-dong Science and Technology Press, 2006.
- 24 E. Laviron, *J. Electroanal. Chem. Interfacial Electrochem.*, 1979, **101**(1), 19–28.
- 25 P. Xiao, C. Bao, Q. Jia, R. Su, W. Zhou and J. Jia, *J. Sep. Sci.*, 2011, **34**, 675–680.
- 26 Y. Y. Han, L. Y. Wang, Y. Y. Zhao, Y. Q. Li and L. Y. Liu, *Chromatographia*, 2013, **76**(23), 1747–1753.
- 27 C. Tong, Y. Guo and W. Liu, *Chemosphere*, 2010, **81**(3), 430–435.
- 28 A. Elbelazi, F. Canfarotta, J. Czulak, M. J. Whitcombe, S. Piletsky and E. Piletska, *Adv. Nano Res.*, 2019, **12**, 3044–3050.
- 29 J. H. Wang, G. Y. Li, X. J. Liu, R. Feng, H. J. Zhang, S. Y. Zhang and Y. H. Zhang, *Inorg. Chim. Acta*, 2018, **473**, 70–74.
- 30 Y. F. Jing, B. F. Long, Q. Huang, Y. Mi, Y. K. Gao and F. L. Hu, *Mater. Chem. Phys.*, 2019, **232**, 152–159.